PCCP

PAPER

View Article Online
View Journal | View Issue

Cite this: *Phys. Chem. Chem. Phys.*, 2015, **17**, 4625

Atomistic simulations of ammonium-based protic ionic liquids: steric effects on structure, low frequency vibrational modes and electrical conductivity†

Anurag Prakash Sunda,*‡ Anirban Mondal‡ and Sundaram Balasubramanian*

Received 18th November 2014,
Accepted 6th January 2015

DOI: 10.1039/c4cp05353b

www.rsc.org/pccp

Protic ionic liquids (PILs) are of great interest as electrolytes in various energy applications. Molecular dynamics simulations of trialkylammonium (with varying alkyl group such as methyl, ethyl, and *n*-propyl) triflate PILs are performed to characterize the influence of the alkyl group on the acidic site (N–H) of the ammonium cation. Spatial distribution function of anions over this site on the cation reveals significant influence of the length of alkyl tail on intermolecular structure. Vibrational density of states and normal modes are calculated for bulk liquids to probe atomic displacements in the far infrared region. The observed N–H···O hydrogen bond stretching vibration in 155–165 cm^{-1} frequency region agrees well with experiments. Trends in electrical conductivity calculated using Nernst–Einstein and Green–Kubo relation are in qualitative agreement with experiments. The self-diffusion coefficient and the electrical conductivity is highest for *N*,*N*-dimethyl-*N*-ethylammonium triflate ([N112][TfO]) and is lowest for *N*,*N*-di-*n*-propyl-*N*-methylammonium triflate ([N133][TfO]) IL.

1 Introduction

Room temperature ionic liquids (ILs) have attracted tremendous interest as electrolytes or dopants in fuel cells, batteries, supercapacitors and solar cells due to their excellent thermodynamic, transport and electrochemical properties.[1–8] Improvement in thermal and electrochemical properties of fuel cells through the use of cost-effective ammonium based protic and aprotic ILs as electrolytes has spurred interest in them.[7,9–15] Nakamoto and Watanabe synthesized a series of protic ILs (PILs) from Brønsted acid–base combination of aliphatic amines with oxoacids. They obtained remarkable electrolytic properties under anhydrous conditions for diethylmethylamine trifluoromethanesulfonic acid ([dema][TfO]) PIL.[10] Lee *et al.*[16] characterized composite polymer electrolyte membranes which were fabricated using [dema][TfO] IL under non-humidified conditions. The authors observed excellent activity for fuel cell (H_2/O_2) reactions at the Pt electrode and improved ionic conductivity using [dema][TfO] IL. Iojoiu and co-workers[17–22] analysed the nanostructuring and transport properties of ammonium based IL doped composite membranes as a function of temperature, hydration and concentration of doped IL. Apart from the improved thermal and mechanical stability of the composite membrane, the presence of cationic and anionic clusters in the membrane matrix was shown to enhance long-range charge transfer. The strength of the Coulomb interactions and polarization forces are critical parameters in determining the orientational correlations of cations and anions as revealed in molecular dynamics study of imidazolium based ILs.[23–25] The sensitivity of cation–anion interactions, size and shape of cations in quaternary ammonium protic ILs is a crucial factor for electrochemical and charge transfer processes. Ludwig and co-workers[26–28] used far infrared and terahertz spectroscopy studies to probe molecular interactions in ILs. The authors characterized the low-frequency region of various ILs and showed that the structure of ILs is largely determined by Coulomb energy, hydrogen bonding and dispersion forces between the ion species. Koh *et al.*[29] analyzed the effect of cation size on the capacitance of electrochemical double layer capacitors using various quaternary ammonium cation based [BF_4^-] salts. They demonstrated that smaller crystallographic ionic radii of ions in trimethylethylammonium and trimethylpropyl-ammonium cations lead to 10% higher capacitance compared to tetraethylammonium cations. Sunda and Venkatnathan[30] investigated the structure and dynamics of benzyltrialkylammonium trifluoromethanesulfonate ILs at varying hydration and demonstrated

Chemistry and Physics of Materials Unit, Jawaharlal Nehru Centre for Advanced Scientific Research, Bangalore 560064, India. E-mail: anurag@jncasr.ac.in, bala@jncasr.ac.in; Fax: +91 (80) 2208 2766; Tel: +91 (80) 2208 2808

† Electronic supplementary information (ESI) available: Non-bonding force field parameters are provided in Table S1. The self-diffusion coefficient of PILs at 300 K from full charge and scaled charge MD simulations are shown in Table S2. Time window for calculating self-diffusion coefficients at 393 K of PILs are given in Table S3. Atom types for methyl/methylene and terminal carbon of alkyl tails are shown in Fig. S1. The cation–cation (N–N) and anion–anion (S–S) RDFs are shown in Fig. S2. A comparison of the structure correlations for [N122][TfO] using the scaled charge model and the full charge model is shown in Fig. S3. For all PILs, a β plot as a function of time for cations and anions is shown in Fig. S4. See DOI: 10.1039/c4cp05353b

‡ These authors contributed equally to this work.

the strong influence of C–H/phenyl interactions on ionic conductivity. MD simulations on neat and hydrated [dema][TfO] IL by Chang *et al.*[31] showed that the ionic conductivity of IL increases with hydration due to enhanced translational and rotational motions of ions. Pulse field gradient stimulated echo NMR spectroscopy on triethylammonium methanesulfonate protic ILs performed by Blanchard *et al.*[32] suggested that proton decoupled transport was absent in the protic IL and the diffusivity of the acidic proton was strongly influenced by the presence of water. Johnson *et al.*[33] studied Pt electrode kinetics as a function of temperature in [dema][TfO] IL for H_2 and O_2 fuels. The authors observed enhanced electrode kinetics in anhydrous IL above 100 °C. Ejigu and Walsh[34] characterized the effect of adsorbed ions on Pt electrodes for [dema][TfO] and dimethylethylammonium trifluoromethanesulfonate ([dmea][TfO]), and diethylmethylammonium bis-(trifluoromethanesulfonyl)imide ([dema][Tf_2N]) ILs. A slower O_2 reduction in [dema][Tf_2N] was observed due to adsorption of [Tf_2N^-] ions on Pt electrodes compared to [dema][TfO] and [dmea][TfO] ILs.

The choice of an alkyl group such as methyl, ethyl or *n*-propyl on trialkylammonium cation leads to a significant variation in proton conductivity and electrochemical properties.[10] Among the several alkyl group combinations, [dema][TfO] IL showed better electrochemical properties compared to other ILs. In the present work, MD simulations are employed to characterize protic ILs (PILs) consisting of a trialkylammonium cation and a [TfO^-] anion. [TfO^-] anion based PILs with varying ammonium cations such as (a) *N*,*N*-dimethyl-*N*-ethylammonium (dmea) triflate ([N112][TfO]), (b) *N*,*N*-diethyl-*N*-methylammonium (dema) triflate ([N122][TfO]), (c) *N*,*N*,*N*-triethylammonium (tea) triflate ([N222][TfO]), and (d) *N*,*N*-di-*n*-propyl-*N*-methylammonium (dpma) triflate ([N133][TfO]) were chosen. This work aims to investigate the influence of steric effects on hydrogen bond interactions due to the size of the alkyl group. Low-frequency vibrational modes and dynamical properties of these PILs are also explored.

2 Computational section

2.1 Simulation details

Cation and the anion of PILs used in the present study are shown in Fig. 1. Classical MD simulations of these protic ILs were carried out using the LAMMPS[36] program. Parameters for bonding interactions were taken from the OPLS-AA force-field.[37]

Table 1 Density (ρ in g cm^{-3}) of ammonium-triflate PILs from *NPT* simulations

T (K)	[N112][TfO]	[N122][TfO]	[N222][TfO]	[N133][TfO]
300	—	1.262[a] (1.277[c])	—	1.192[b] (1.203[c])
313	—	1.251 (1.262[c])	—	1.184 (1.189[c])
393	1.236	1.184	1.139	1.118

[a] ρ = 1.299 calculated using full atomic charges for [N122][TfO] at 300 K. [b] ρ = 1.218 calculated using full atomic charges for [N133][TfO] at 300 K. [c] Experimental data from ref. 35.

For the non-bonding interactions, van der Waals parameters were taken from the work of Chang *et al.*[31] which were refined by the authors from the original AMBER force field values, in order to reproduce experimental density. Based on condensed-phase quantum calculations, we have shown that the ions in imidazolium based ILs realistically can be modeled with a fractional charge (less than unity).[38] For instance, the charge on ions in such salts containing triflate ($CF_3SO_3^-$) as the anion was $\pm 0.78e$. Assuming a similar charge transfer in PILs, the ion charges in the current simulations have been scaled down by a factor of 0.78 from the original values.[39,40] Simulations with full atomic charges (at 300 K) slightly overestimate the density of PILs as shown in Table 1, and the diffusion coefficient (at 300 K) is found to be lower by an order of magnitude than either that of simulations with scaled charge or experiments (see Table S2 of ESI†).

All the systems were simulated using 256 ion pairs. The Packmol[41] software package was used to set up the initial configurations. Particle–particle particle-mesh (PPPM) solver was used to compute the long-range electrostatic interactions with a precision of 10^{-5}. A distance cutoff of 11 Å was employed to calculate the pairwise interactions in real space. Equations of motion were integrated using the velocity Verlet algorithm with a time step of 1 fs. All C–H covalent bonds were constrained using the SHAKE algorithm as implemented in LAMMPS.[36] Standard Lorentz–Berthelot rules were applied to derive the cross interactions between different atom types. Long-range corrections were applied while calculating the energy and pressure. The Nosé–Hoover thermostat[42,43] and barostat with the extended Lagrangian approach were employed for constant temperature and constant pressure dynamics with a damping factor of 1 ps. MD simulations were performed at three different temperatures 300 K, 313 K and 393 K. The energy minimization of 256 ion-pairs was followed by an equilibration of 12 ns in the *NPT* ensemble. A production run of 32 ns was generated in the

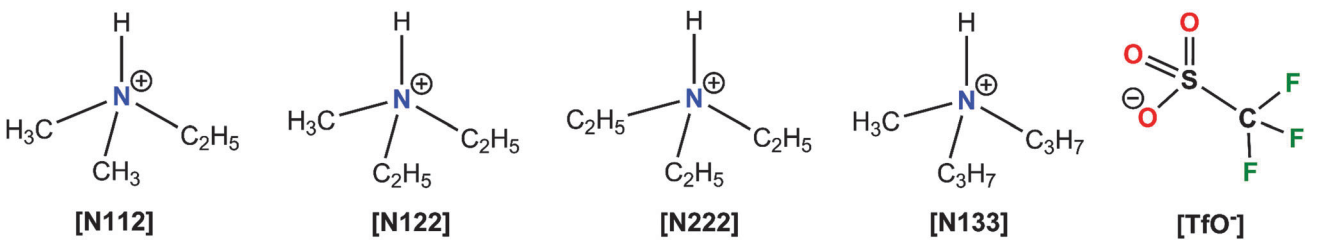

Fig. 1 Ammonium cations (a) *N*,*N*-dimethyl-*N*-ethylammonium ([N112]), (b) *N*,*N*-diethyl-*N*-methylammonium ([N122]), (c) *N*,*N*,*N*-triethylammonium ([N222]), (d) *N*,*N*-di-*n*-propyl-*N*-methylammonium ([N133]), and (e) triflate ([TfO^-]) anion.

NVT ensemble and was further used to calculate the structural and dynamical properties of these protic ILs.

The computed densities from *NPT* simulations (see Table 1) were close to experiment, (within 2% error) as reported for [N112][TfO] IL and [N133][TfO] IL.[35] The density decreases with an increase in temperature from 300 K to 393 K. At 393 K, the density decreases with an increase in the molecular weight of the ammonium cation or IL. Simulations were also carried out at 393 K, so as to compare with experimentally determined diffusion coefficients of ions and the electrical conductivity of ILs.

2.2 Vibrational density of states (VDOS)

A different set of simulations was performed for all the systems, each consisting of 100 ion-pairs. The simulation temperature was 393 K. Each system was equilibrated for 5 ns in the *NPT* ensemble which was followed by a 10 ns production run in the *NVT* ensemble. Atom coordinates were stored every 100 ps to obtain 100 snapshots for each PIL. Other details of the simulations are the same as discussed in the previous section for 256 ion-pair systems.

An efficient conjugate gradient method as implemented in LAMMPS was employed to minimize the 100 configurations obtained from the classical MD trajectory for each ionic liquid. The Hessian matrix of the potential energy with respect to the atom coordinates was calculated using a normal-mode analysis (NMA) code developed earlier within our group.[44] The eigenvectors of the Hessian are related to atomic displacements in a mode and the eigenvalues correspond to the frequencies. A 2 cm^{-1} bin width was used to calculate the frequency spectrum which was averaged over all the 100 quenched configurations.

The VDOS can also be obtained as the Fourier transforms of the time autocorrelation function of the atomic velocities (VACF). This can be defined as

$$I(\omega) = \frac{1}{k_B T}\sum_j m_j\left[\frac{1}{2\pi}\int_{-\infty}^{\infty}\exp(-i\omega t)\langle \mathbf{v}_j(0)\cdot\mathbf{v}_j(t)\rangle \mathrm{d}t\right] \quad (1)$$

where $\mathbf{v}_j(t)$ is the velocity of atom type j at time t. In order to calculate this VACF, a separate MD trajectory was generated for 100 ps and atomic velocities were stored at each time step.

VMD[45] and Jmol[46] were used to visualize all the systems. Atomic displacements were visualized in Jmol[46] for the assignment of different modes present in the systems.

2.3 Electrical conductivity

The electrical conductivity, σ_{GK}, was calculated through the equilibrium Green–Kubo relation using the time integral of the electric-current autocorrelation function defined as[47,48]

$$\sigma_{GK} = \frac{1}{3k_B TV}\int_0^{\infty}\langle \mathbf{j}(t)\cdot\mathbf{j}(0)\rangle \mathrm{d}t, \quad (2)$$

where $\mathbf{j}(t)$ is the electric-current,

$$\mathbf{j}(t) = \sum_{i=1}^{N} q_i \mathbf{v}_i(t) \quad (3)$$

and q_i and $\mathbf{v}_i(t)$ represent the charge and velocity of atom i at time t. N is the total number of atoms in the system. Atom velocities were stored at every time step from sixteen independent MD runs, each of length of 2 ns. Each trajectory was used to calculate the electric current autocorrelation function and these were then averaged over trajectories.

It is also possible to calculate the ionic conductivity within the approximation of independent ion motion using the Nernst–Einstein relation,[48]

$$\sigma_{NE} = \frac{N_i q^2}{Vk_B T}(D^+ + D^-) \quad (4)$$

where V is the volume, T is the temperature, N_i is the number of ion-pairs, q is the effective net charge of the ions and k_B is the Boltzmann constant.

3 Results and discussions

PILs used in the present study exhibit various interionic interactions including hydrogen bonding due to the presence of the acidic site on the ammonium cation. The steric effects of alkyl groups on the cation center, cationic symmetry and hydrogen bond interactions play vital roles in determining the intermolecular structure and thus dynamics in PILs. We have calculated radial distribution functions (RDFs), spatial distribution functions (SDFs) and vibrational spectrum in the low-frequency region to characterize these PILs.

3.1 Radial distribution functions

RDFs for various interionic interactions are shown in Fig. 2 and 3. The N–S RDF (see Fig. 2a) show a bifurcated peak at 4 Å and 5.5 Å with a large solvation shell of 8 Å and a small shoulder with a lower rise around 7 Å. The first peak in N–S RDF at ~4 Å is due to the strong hydrogen bond interaction between the acidic site of the quaternary ammonium cation (N–H) and oxygen atoms of anions within the first solvation shell and the peak height is highest for [N133][TfO] IL. These cation–anion hydrogen bond interactions within ~4 Å are revealed from the O–H RDF (see Fig. 2b) which shows an intense peak around 2 Å. The peak height of O–H RDF increases with an increase in the bulky nature of an alkyl group on the cation from the methyl to *n*-propyl group. This peak profile of O–H RDF for various PILs exhibits a qualitative similarity to the first peak of N–S RDF. Thus, the cation–anion hydrogen bond interactions within ~4 Å distance suggest that anions prefer to approach from the top direction (*i.e.* along the N–H bond vector) of the cation. The second peak in N–S RDF at ~5.5 Å is due to weak hydrogen bond interactions between terminal methyl hydrogen atoms and anion oxygen atoms which occur at larger distances. The peak height decreases from [N112][TfO] to [N222][TfO] but is found to be much higher for [N133][TfO]. Such an unusual peak profile can be understood by examining the RDFs between methyl/methylene hydrogen atoms of the quaternary ammonium cation and anion oxygen atoms (see Fig. 3a). The interactions of anion oxygen atoms with methyl/methylene hydrogen atoms are strongest in [N133][TfO] and

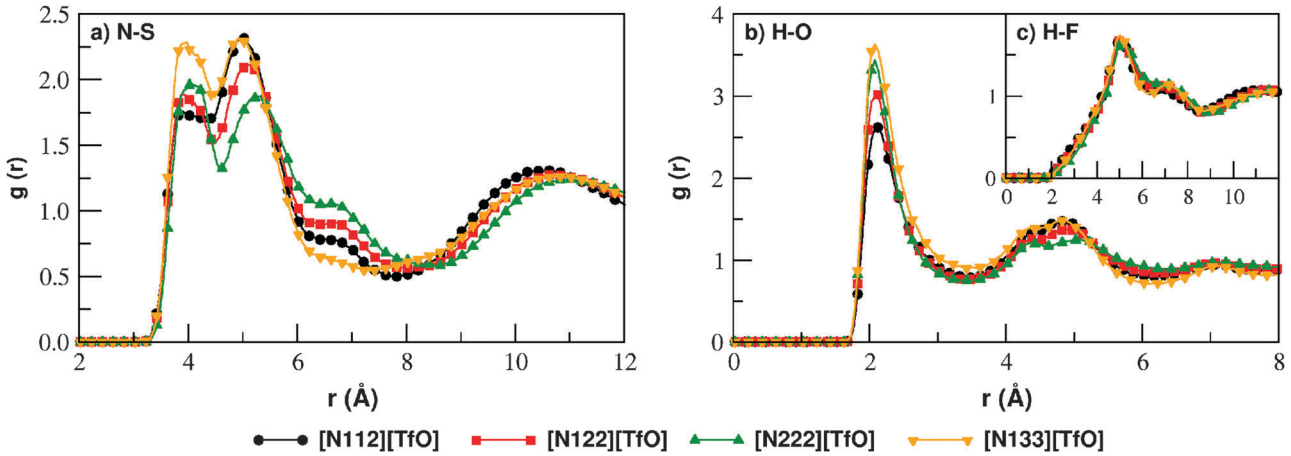

Fig. 2 RDFs for cation–anion (a) N–S, and hydrogen bond interactions of acidic hydrogen (H_N) with [TfO^-] anion (b) H–O, and (c) H–F.

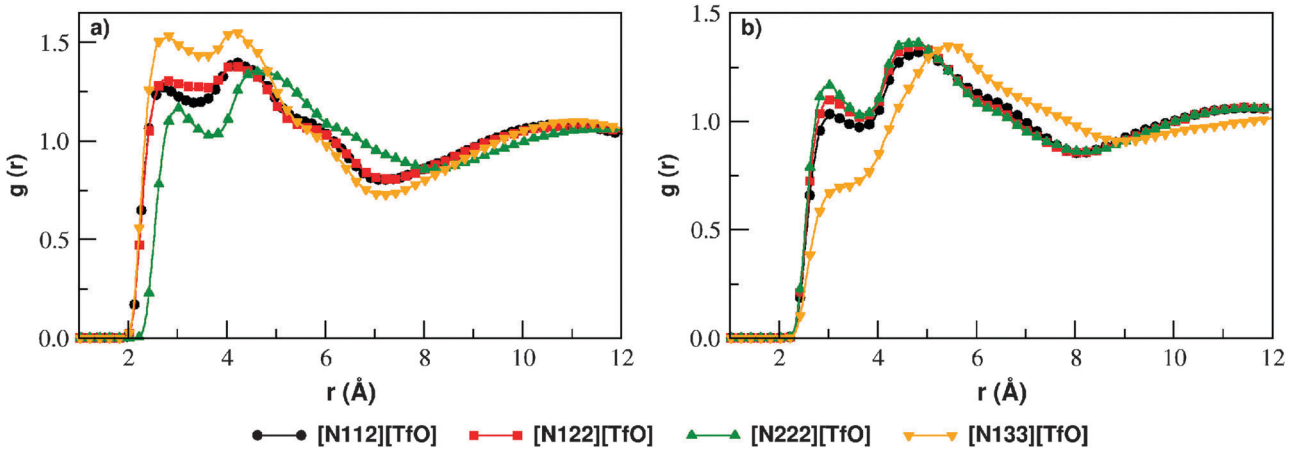

Fig. 3 RDFs between (a) methyl/methylene hydrogen atoms, and (b) terminal alkyl (ethyl/propyl) hydrogen atoms of ammonium cation and anion oxygen atoms (see Fig. S1 of ESI† for the description of atom types for methyl/methylene and terminal carbon of alkyl tails).

weakest in [N222][TfO]. A bifurcated peak at 5.5 Å is seen in the N–S RDF (Fig. 2a). Thus, the approach of anions towards the cationic center from the methyl group side is restricted in [N222][TfO] IL due to the presence of more symmetric and bulky ethyl groups. However, such weak hydrogen bond interactions between terminal propyl H-atoms and anion oxygen atoms (in [N133][TfO]) are completely absent as seen from Fig. 3b. The steric hindrance due to propyl chain limits the possibility of anion distribution over the propyl chain. Nevertheless, the weak hydrogen bond interactions between terminal ethyl H-atoms and anion oxygen atoms are highest in [N222][TfO] due to the presence of more symmetric terminal hydrogen atoms. Hence, the RDF peak profile for terminal H-atoms of the ethyl/propyl tail and anion oxygen atoms reveals the characteristics of cation–anion interactions (seen from N–S RDF) at a larger distance of 7 Å. These hydrogen bond interactions between various sites of cation and anions can be seen from a snapshot of triflate anion clusters around the ammonium cation (see Fig. 4). The hydrogen bond distance along the N–H bond vector is similar to that seen from the RDFs (Fig. 2b). To summarize, the O–H hydrogen bonding (albeit a weak one) propensity increases with an increase in the alkyl tail length and depends critically on the symmetry of the cation as well. The coordination number for the N–S and O–H RDFs decreases with an increase in the length of the alkyl group on the cation from the methyl to *n*-propyl group (see Table 2). However, hydrogen bond interactions between acidic hydrogen (N–H) of the cation and fluorine atoms of the anion are not observed (see Fig. 2c). The cation–cation interactions from N–N RDF (see Fig. S2(a) of ESI†) show a broad peak (5 to 9 Å). The peak position is shifted towards larger distance with an increase in the length of the alkyl group on the cation. Similar to the cation–cation $g(r)$, the S–S RDF (see Fig. S2(b) of ESI†) shows a broad peak (5 to 10 Å). Fig. S3 of ESI† shows that the structural correlations calculated for [N122][TfO] using the reduced charge model well reproduce those from the full charge model reported by Chang *et al.*[31] Although the O–H $g(r)$ shows some difference, the running coordination number shows no change within the first shell from the results of the full charge simulations[31] as shown in the inset of Fig. S3(d) of ESI.† Thus, the trends seen in structural correlations for PILs are valid regardless of the use of a reduced charge model.

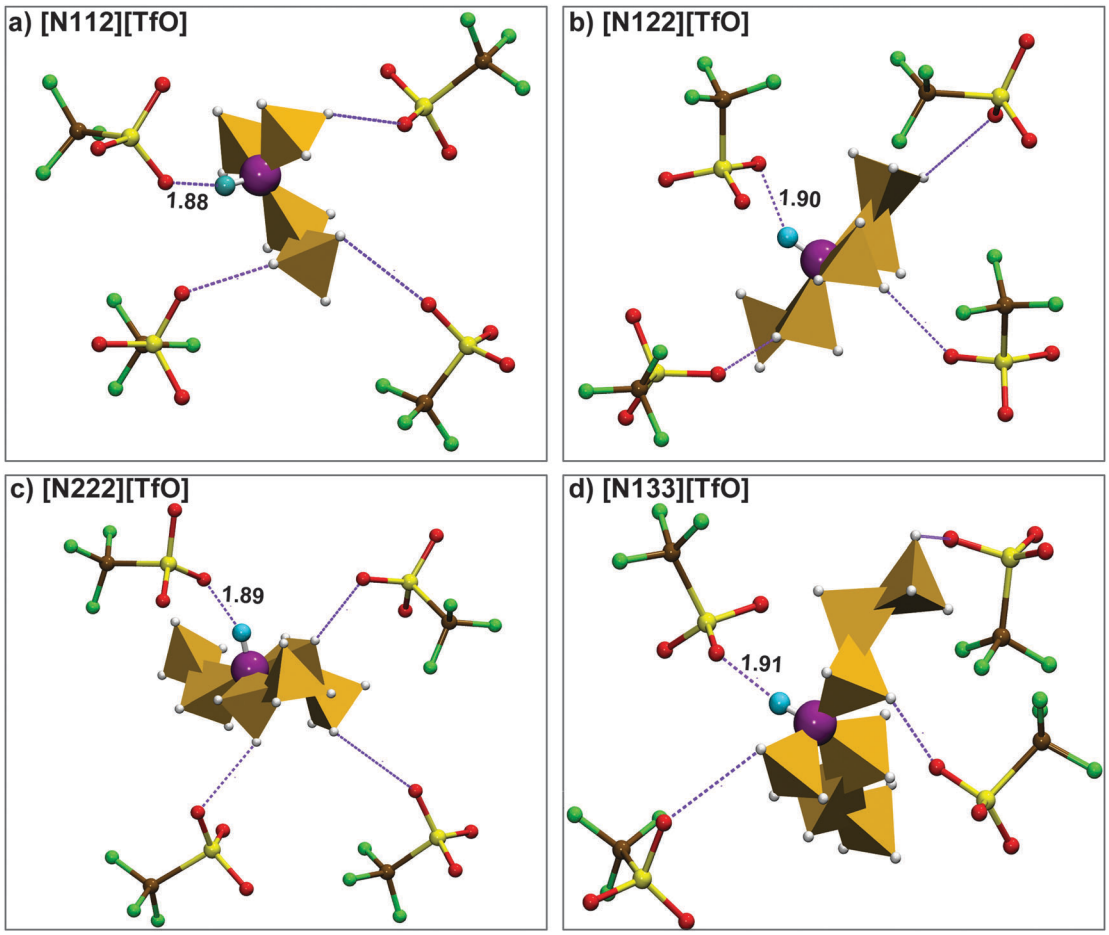

Fig. 4 Snapshots for ammonium-triflate ILs from *NVT* production run showing cation–anion interactions. The N–H···O hydrogen bond distance (in Å) is representative of the O–H distance. Snapshots are arbitrarily chosen based on the O–H distance and hence, the distance for the possible C–H···O interaction (dashed line) is not displayed. [Color scheme (i) cation: N – purple (CPK), H_N – cyan (CPK), C – orange (polyhedra), alkyl H – white (CPK), and (ii) anion (CPK): C – ochre, F – green, S – yellow, oxygen – red.]

Table 2 Coordination numbers for cation–anion and hydrogen bond interactions in the first solvation shell of PILs

ILs	[N112][TfO]	[N122][TfO]	[N222][TfO]	[N133][TfO]
N–S (at 8.0 Å)	7.0	6.5	6.2	5.3
O–H_N (at 3.5 Å)	2.0	1.8	1.7	1.8
O–H_m (at 7.0 Å)	15.2	13.7	12.8	11.9
O–H_t (at 8.0 Å)	22.2	20.0	18.2	17.6

Furthermore, these structural observations are validated by calculating SDFs for these PILs. The SDFs calculated for the S-atom and the O-atom of anions around the N-atom of the cation are shown in Fig. 5. The spatial density map of anions around the center of mass of the cation shows that the most preferred binding site of anions is opposite to the acidic proton. The distribution of anions along the N–H bond vector shows that the density map became more condensed and tapered over the quaternary ammonium acidic proton with an increase in the bulky nature of the cation. Whereas, the spatial density map of anions over alkyl terminals of the cation is highly diffused in [N112][TfO] IL which becomes scattered in [N122][TfO] and [N222][TfO] PILs respectively. In the case of [N133][TfO] IL, the steric-hindrance due to the propyl chain limits the anion distribution over the terminal propyl group of the cation. The spatial density map of anions around the quaternary ammonium cation is more symmetric in [N222][TfO] compared to other PILs.

3.2 Velocity autocorrelation function and low frequency vibrational modes

In order to characterize the dynamical processes in PILs, the center of mass velocity autocorrelation function (VACF) for cations and anions was calculated (see Fig. 6). The first minimum is found to be deepest for the cation in [N112][TfO] (see inset of Fig. 6a). The well depth decreases significantly with an increase in the bulkiness of alkyl tails on the quaternary ammonium cation and becomes insubstantial/or shallow in [N133][TfO] IL. The influence of the alkyl group attached to the quaternary ammonium ion on the exponential decay of the triflate anion VACF is minimal and found to be similar for all the ILs. The variations in caging as seen from cation VACF

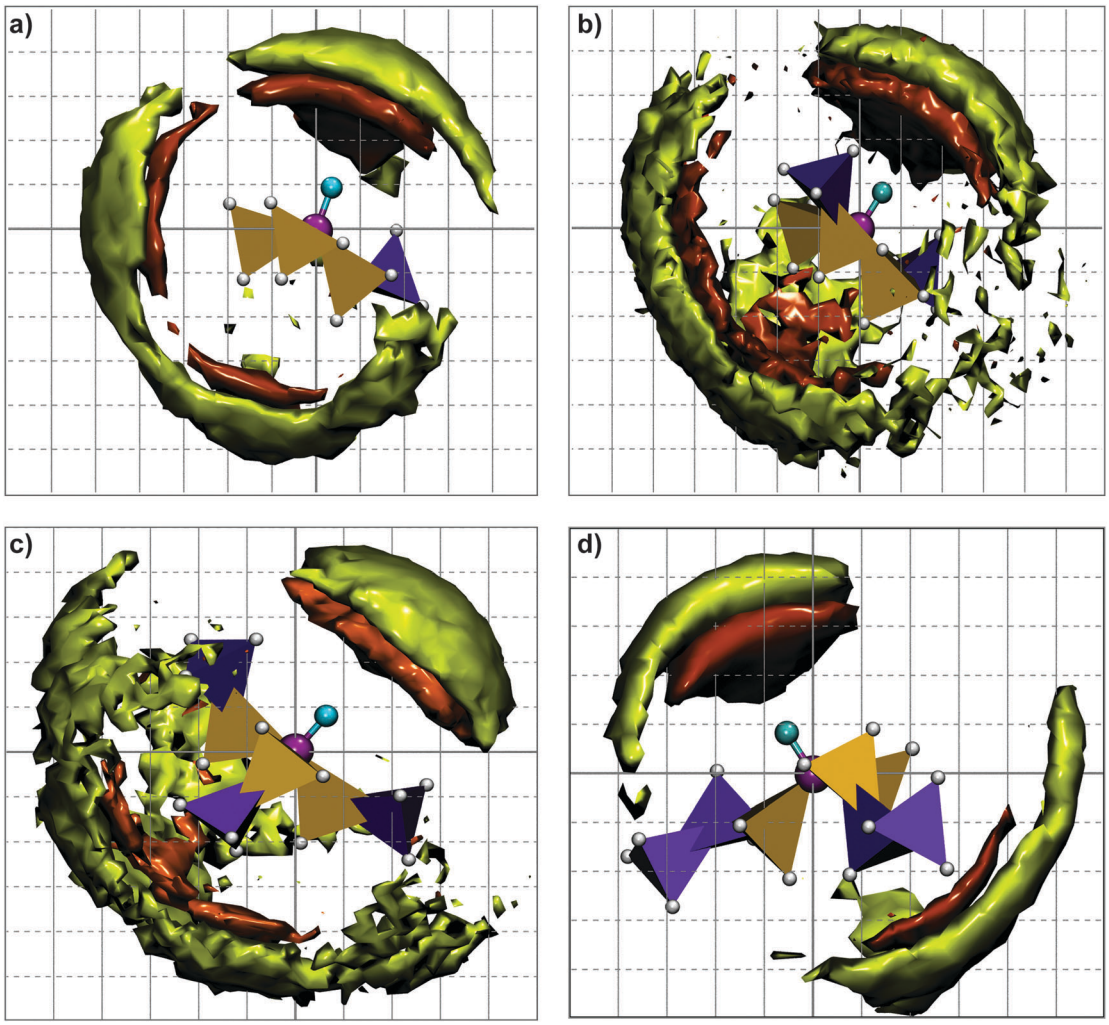

Fig. 5 Spatial density map of anions (S-atom and O-atoms) around the center of mass of the ammonium cation calculated from MD simulation at 393 K for (a) [N112][TfO], (b) [N122][TfO], (c) [N222][TfO], and (d) [N133][TfO] PILs. [(i) Colour scheme for cation: N – purple (CPK), H_N – cyan (CPK), C_{methyl} – orange (polyhedra), $C_{ethyl/propyl}$ – violet (polyhedra), alkyl H-white (CPK), and for anion iso-surface: S – yellow-green, O – orange-red; (ii) iso-surface value is 0.005 $Å^{-3}$ for [N112][TfO], [N133][TfO], and 0.006 $Å^{-3}$ for [N122][TfO], [N222][TfO] respectively.]

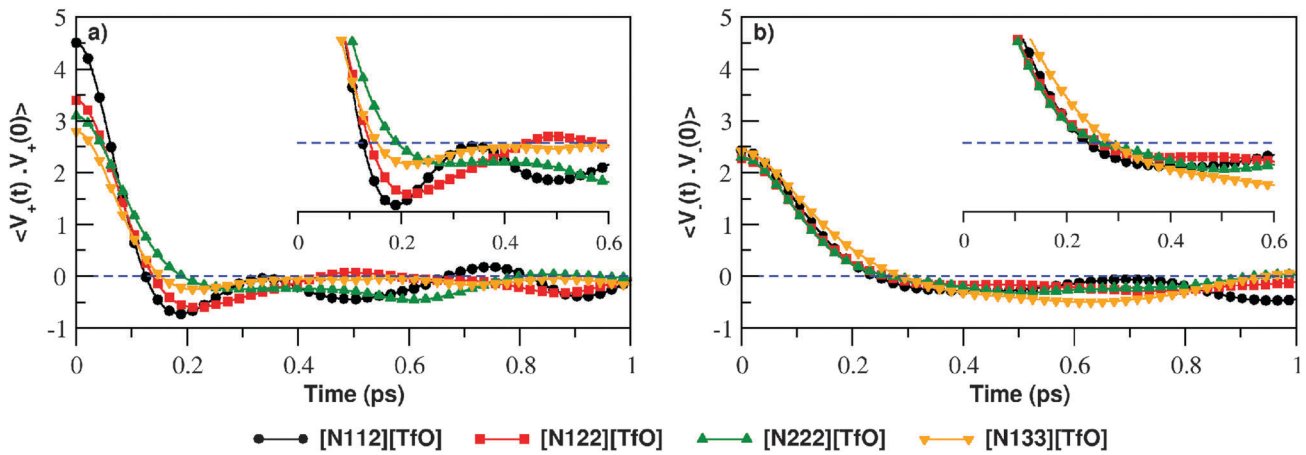

Fig. 6 Center of mass velocity autocorrelation functions for (a) quaternary ammonium cations, and (b) triflate anions, respectively, at 393 K (insets show initial decay).

suggests that the rattling motions are expected to be significant in [N112][TfO] IL.

The dynamics of PILs is further probed by examining the vibrational density of states (VDOS). The vibrational spectrum is calculated from the Fourier transform of the VACF (see Fig. 7a). A broad peak in the low-frequency region corresponding to the collision frequency of inter-molecular modes is observed. As expected, the peak height is highest for [N112][TfO] IL. Additionally, low intensity peaks are also observed in the 200–350 cm^{-1} region of VDOS which show a red shift with an increase in the bulkiness of the alkyl group on the quaternary ammonium cation. Fumino *et al.*[26,27] have characterized the low-frequency vibrational modes using far-infrared spectroscopy (FIR) for various quaternary ammonium based PILs with [NO_3^-], [$CH_3SO_3^-$], and [$CF_3SO_3^-$] anions. They detected low-frequency vibrational bands (100–400 cm^{-1}) due to the presence of inter-molecular interactions in PILs and assigned the vibrational bands at 100 cm^{-1}, 154–160 cm^{-1} and ~400 cm^{-1} region to unspecific librational motions, $^+$N–H···anion interactions, and bending modes of cation respectively. To dissect the contribution of intermolecular interactions in the low-frequency vibrational band of PILs as seen from VDOS, we have carried out normal-mode analysis (NMA). Fig. 7b displays atomic displacements (obtained from eigenvectors of the Hessian matrix) of a few modes in the PILs using the empirical force field. The atomic displacements obtained using NMA in the low frequency region of 40–100 cm^{-1} are mainly due to the rattling motions of anions. For example, the vibrational modes present in the [N133][TfO] at 51 cm^{-1} are shown in Fig. 8a, where the [TfO^-] anions mainly contribute to the modes. The acidic protons (N–H) mainly contribute to the vibrational modes in the frequency range 155–165 cm^{-1}. For example, the N–H···O stretching modes of the hydrogen bond in [N133][TfO] occurs at 161 cm^{-1} as depicted in Fig. 8b. The low intensity peaks in the 200–350 cm^{-1} region (see Fig. 7b) corresponds to the twisting modes of the quaternary ammonium ion. Similar to the VDOS of the cation, the peak intensity shows a red shift with an increase in the length of the alkyl group in the quaternary ammonium cation. For example, the twisting mode of the quaternary ammonium ion in [N133][TfO] occurs at 221 cm^{-1} as shown in Fig. 8c. Results from MD simulations agree well with experimental observations of Fumino *et al.*[26,27] on PILs.

3.3 Self-diffusion coefficient and electrical conductivity

The influence of the quaternary ammonium triflate structure on the dynamical properties of PILs with varying alkyl groups on the cation is investigated by calculating the mean square displacement (MSD) and electrical conductivity. For all PILs, the MSD for cations and anions are calculated using the Einstein relationship. To identify the diffusive regime of ILs, the exponent β is determined using eqn (5)[2,49] as:

$$\beta(t) = \frac{d \ln\langle \Delta r^2(t) \rangle}{d \ln(t)} \quad (5)$$

where $\beta(t)$ is the first derivative of log MSD *versus* log time plot. For diffusive behaviour, $\beta(t)$ = 1. $\beta(t)$ plots for cations and anions (see Fig. S4 of ESI†) show diffusive behavior of ILs beyond 2 ns. The self-diffusion coefficients (D^+ and D^- for cations and anions respectively) are calculated from the diffusive regime (see Table S3 of ESI†) of MSD.

The calculated D^+ and D^- values at 393 K are shown in Table 3. For all PILs, the diffusivity of cations (D^+) is higher compared to that of triflate anions in respective ILs. The self-diffusion coefficient (D^+) of the quaternary ammonium cation decreases with an increase in the bulkiness and molecular mass of the cation. A strong influence of the bulky nature of the cation is observed on the mobility of triflate anions. For example, the D^- in [N133][TfO] decreases by a factor of 0.6 compared to that in [N122][TfO]. The Nernst–Einstein conductivity calculated from D^+ and D^- decreases with an increase in the length of the alkyl group on the cation. The electrical conductivity calculated from the Green–Kubo relation shows large deviations (>60%) with experimental values[10] and points

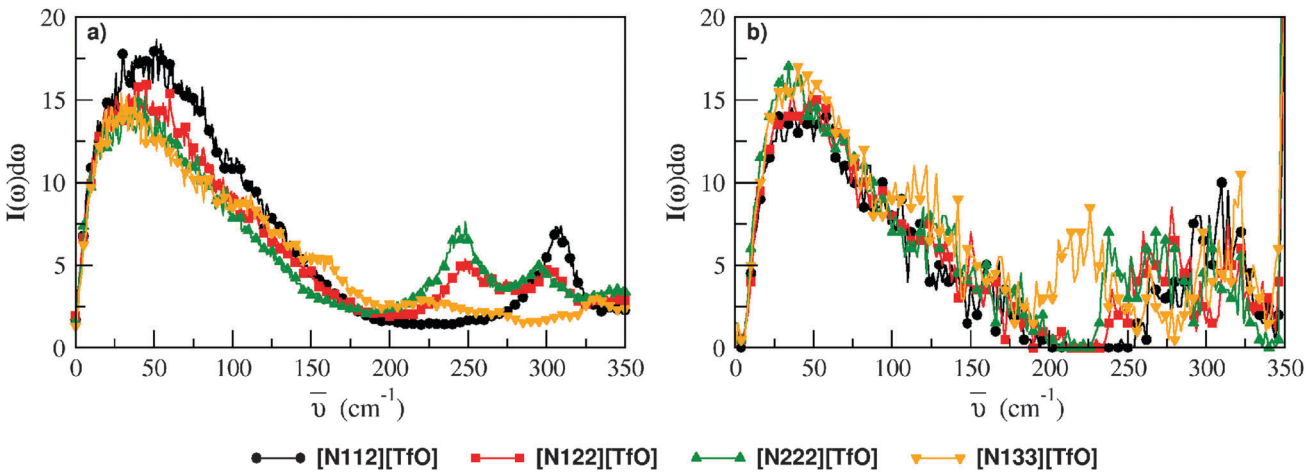

Fig. 7 Vibrational density of states (VDOS) calculated for ILs at 393 K from (a) the power spectrum of the velocity autocorrelation function (VACF), and (b) normal-mode analysis (NMA) within the harmonic approximation.

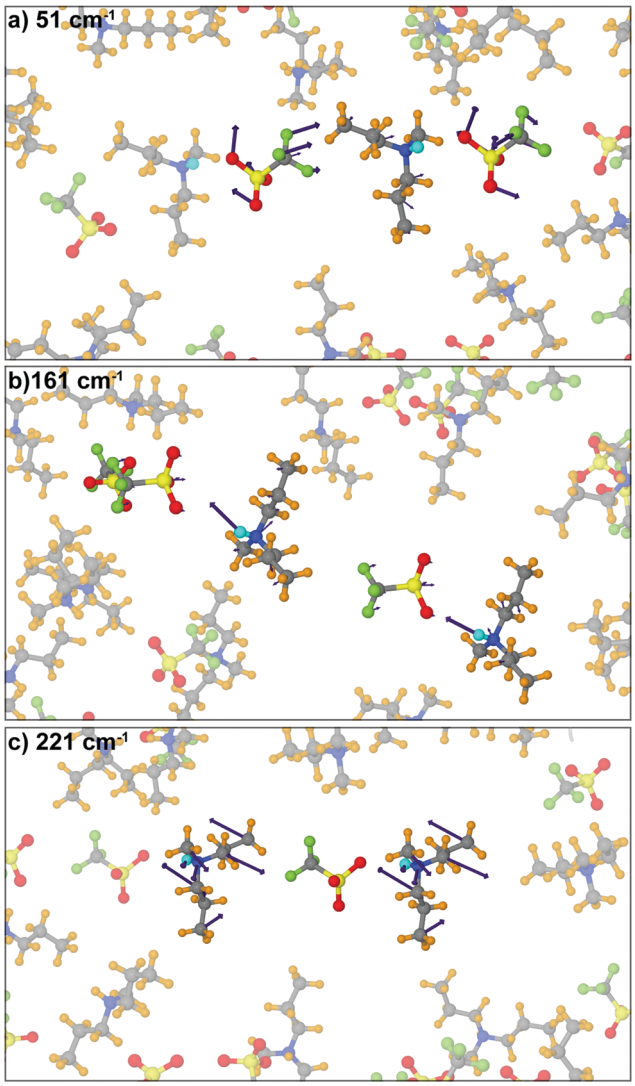

Fig. 8 Atomic displacements in [N133][TfO] IL (a) interionic modes at 51 cm^{-1}, (b) stretching vibration of the N–H···O hydrogen bond at 161 cm^{-1}, and (c) twisting modes of the cation center at 221 cm^{-1}. Here, only a few ions are highlighted out of the bulk liquid for the sake of clarity. Arrows represent atomic displacement vector and are scaled by an arbitrary factor for better visualization. [Color scheme for cation (CPK): N – blue, H_N – cyan, C – gray, alkyl H – orange, and for anion: C – gray, F – green, S – yellow, O – red.]

to the necessity of refinement of the force field, particularly the non-bonded parameters. The difference between the conductivity obtained from the Green–Kubo relation compared to that obtained from the Nernst–Einstein relation indicates that the dynamics of these PILs is highly correlated. In summary, the self-diffusion coefficient and the electrical conductivity (σ_{NE} and σ_{GK}) from simulations is highest for [N112][TfO] and is lowest for [N133][TfO]. Although the σ_{GK} values are lower then σ_{Exp},[10] the trend among the PILs is captured from these simulations. A quantitative comparison can be expected with a refined force field.

Table 3 Self-diffusion coefficients ($\times 10^{-6}$ cm^2 s^{-1}) and electrical conductivity (S m^{-1}) of ammonium-triflate ILs from MD simulations at 393 K

	Conductivity (S m^{-1})					
System	D^+	D^-	σ_{NE}	σ_{GK}	$\sigma_{Exp.}$[10]	σ_{GK}/σ_{NE}
[N112][TfO]	2.9	2.2	4.8	1.9	5.60	0.39
[N122][TfO]	2.5	2.0	3.9	1.6	4.33	0.41
[N222][TfO]	2.2	1.7	3.0	0.9	2.76	0.29
[N133][TfO]	1.5	1.2	2.0	0.7	—	0.37

4 Conclusions

A molecular level understanding of structure and dynamics in quaternary ammonium triflate PILs is presented using classical MD simulations. RDFs demonstrate that hydrogen bonding interactions between the ions increase with an increase in the bulkiness of the alkyl group attached to the N-atom of the ammonium cation. Weak hydrogen bonding between ethyl hydrogen atoms and anion oxygen atoms lead to a more symmetric distribution of anions in [N222][TfO]. The spatial density map of anions over alkyl terminals of the cation varies from highly diffused (in [N112][TfO]), scattered (in [N122][TfO] and [N222][TfO]) to condensed (in [N133][TfO]), with an increase in size of the alkyl group from methyl to *n*-propyl. The depth at the first minimum of VACF is highest for [N112][TfO] and becomes insubstantial for [N133][TfO]. The VDOS calculated from the Fourier transform of VACFs clearly shows the presence of strong intermolecular interactions. Furthermore, normal-mode analysis (NMA) within the harmonic approximation distinctly reveals N–H···O hydrogen bond stretching vibration in the low frequency region of 155–165 cm^{-1}. A red shift in twisting vibration modes of the quaternary ammonium cation is observed in the 200–350 cm^{-1} region with an increase in the bulkiness of the alkyl group from methyl to *n*-propyl. Anion rattling modes are present in the sub-100 cm^{-1} region.

The influence of steric effects on ionic mobility is examined by calculating the self-diffusion coefficient and electrical conductivity. A significant improvement in the prediction of self-diffusion coefficient is seen with the scaled charge model compared to the full charge model, which is compared for the case of [N122][TfO] to experimental values. The mobility of ions decreases with an increase in the size of the alkyl group. A large difference (>60%) in electrical conductivity calculated from the Green–Kubo relation compared with that obtained from the Nernst–Einstein relation points to the correlated nature of ion transport in PILs. The force field for the simulations needs to be refined in order to quantitatively reproduce experimentally determined electrical conductivity values, although its trend upon changing the cation is well reproduced by the simulations. Furthermore, *ab initio* MD simulations and/or simulations using polarizable force fields too should be explored for these ammonium ion based protic ILs.

Acknowledgements

We thank DST for support. This work used the computing resources provided by JNCASR and Center for Development of

Advanced Computing, Bangalore. APS and AM acknowledge JNCASR for financial support. SB thanks Sheikh Saqr Laboratory, JNCASR for a senior fellowship.

References

1 C. A. Angell, N. Byrne and J.-P. Belieres, *Acc. Chem. Res.*, 2007, **40**, 1228–1236.
2 E. J. Maginn, *Acc. Chem. Res.*, 2007, **40**, 1200–1207.
3 D. R. MacFarlane, M. Forsyth, P. C. Howlett, J. M. Pringle, J. Sun, G. Annat, W. Neil and E. I. Izgorodina, *Acc. Chem. Res.*, 2007, **40**, 1165–1173.
4 T. L. Greaves and C. J. Drummond, *Chem. Rev.*, 2008, **108**, 206–237.
5 Y. Bai, Y. Cao, J. Zhang, M. Wang, R. Li, P. Wang, S. M. Zakeeruddin and M. Grätzel, *Nat. Mater.*, 2008, **7**, 626–630.
6 M. Armand, F. Endres, D. R. MacFarlane, H. Ohno and B. Scrosati, *Nat. Mater.*, 2009, **8**, 621–628.
7 D. R. MacFarlane, N. Tachikawa, M. Forsyth, J. M. Pringle, P. C. Howlett, G. D. Elliott, J. H. Davis, M. Watanabe, P. Simon and C. A. Angell, *Energy Environ. Sci.*, 2014, **7**, 232–250.
8 M. V. Fedorov and A. A. Kornyshev, *Chem. Rev.*, 2014, **114**, 2978–3036.
9 M. Yoshizawa, W. Xu and C. A. Angell, *J. Am. Chem. Soc.*, 2003, **125**, 15411–15419.
10 H. Nakamoto and M. Watanabe, *Chem. Commun.*, 2007, 2539–2541.
11 J.-P. Belieres, D. Gervasio and C. A. Angell, *Chem. Commun.*, 2006, 4799–4801.
12 J.-P. Belieres and C. A. Angell, *J. Phys. Chem. B*, 2007, **111**, 4926–4937.
13 J. Luo, O. Conrad and I. F. J. Vankelecom, *J. Mater. Chem.*, 2012, **22**, 20574–20579.
14 M. Kumar and A. Venkatnathan, *J. Phys. Chem. B*, 2013, **117**, 14449–14456.
15 H. N. Sarode, G. E. Lindberg, Y. Yang, L. E. Felberg, G. A. Voth and A. M. Herring, *J. Phys. Chem. B*, 2014, **118**, 1363–1372.
16 S.-Y. Lee, A. Ogawa, M. Kanno, H. Nakamoto, T. Yasuda and M. Watanabe, *J. Am. Chem. Soc.*, 2010, **132**, 9764–9773.
17 V. Di Noto, E. Negro, J.-Y. Sanchez and C. Iojoiu, *J. Am. Chem. Soc.*, 2010, **132**, 2183–2195.
18 V. Di Noto, M. Piga, G. A. Giffin, S. Lavina, E. S. Smotkin, J.-Y. Sanchez and C. Iojoiu, *J. Phys. Chem. C*, 2011, **116**, 1361–1369.
19 V. Di Noto, M. Piga, G. A. Giffin, S. Lavina, E. S. Smotkin, J.-Y. Sanchez and C. Iojoiu, *J. Phys. Chem. C*, 2011, **116**, 1370–1379.
20 R. Sood, C. Iojoiu, E. Espuche, F. Gouanvé, G. Gebel, H. Mendil-Jakani, S. Lyonnard and J. Jestin, *J. Phys. Chem. C*, 2012, **116**, 24413–24423.
21 D. Langevin, Q. T. Nguyen, S. Marais, S. Karademir, J.-Y. Sanchez, C. Iojoiu, M. Martinez, R. Mercier, P. Judeinstein and C. Chappey, *J. Phys. Chem. C*, 2013, **117**, 15552–15561.
22 R. Sood, C. Iojoiu, E. Espuche, F. Gouanvé, G. Gebel, H. Mendil-Jakani, S. Lyonnard and J. Jestin, *J. Phys. Chem. C*, 2014, **118**, 14157–14168.
23 T.-M. Chang and L. X. Dang, *J. Phys. Chem. A*, 2009, **113**, 2127–2135.
24 M. Kohagen, M. Brehm, J. Thar, W. Zhao, F. Müller-Plathe and B. Kirchner, *J. Phys. Chem. B*, 2011, **115**, 693–702.
25 C. Schroder, *Phys. Chem. Chem. Phys.*, 2012, **14**, 3089–3102.
26 K. Fumino, E. Reichert, K. Wittler, R. Hempelmann and R. Ludwig, *Angew. Chem., Int. Ed.*, 2012, **51**, 6236–6240.
27 K. Fumino, V. Fossog, K. Wittler, R. Hempelmann and R. Ludwig, *Angew. Chem., Int. Ed.*, 2013, **52**, 2368–2372.
28 K. Fumino, S. Reimann and R. Ludwig, *Phys. Chem. Chem. Phys.*, 2014, **16**, 21903–21929.
29 A. R. Koh, B. Hwang, K. Chul Roh and K. Kim, *Phys. Chem. Chem. Phys.*, 2014, **16**, 15146–15151.
30 A. P. Sunda, V. M. Dhavale, S. Kurungot and A. Venkatnathan, *J. Phys. Chem. B*, 2014, **118**, 1831–1838.
31 T. M. Chang, L. X. Dang, R. Devanathan and M. Dupuis, *J. Phys. Chem. A*, 2010, **114**, 12764–12774.
32 J. W. Blanchard, J.-P. Belières, T. M. Alam, J. L. Yarger and G. P. Holland, *J. Phys. Chem. Lett.*, 2011, **2**, 1077–1081.
33 L. Johnson, A. Ejigu, P. Licence and D. A. Walsh, *J. Phys. Chem. C*, 2012, **116**, 18048–18056.
34 A. Ejigu and D. A. Walsh, *J. Phys. Chem. C*, 2014, **118**, 7414–7422.
35 T. Yasuda, H. Kinoshita, M. S. Miran, S. Tsuzuki and M. Watanabe, *J. Chem. Eng. Data*, 2013, **58**, 2724–2732.
36 S. Plimpton, *J. Comput. Phys.*, 1995, **117**, 1–19.
37 W. L. Jorgensen, D. S. Maxwell and J. Tirado-Rives, *J. Am. Chem. Soc.*, 1996, **118**, 11225–11236.
38 A. Mondal and S. Balasubramanian, *J. Phys. Chem. B*, 2014, **118**, 3409–3422.
39 J. N. Canongia Lopes, J. Deschamps and A. A. H. Pádua, *J. Phys. Chem. B*, 2004, **108**, 2038–2047.
40 J. N. Canongia Lopes and A. A. H. Pádua, *J. Phys. Chem. B*, 2004, **108**, 16893–16898.
41 L. Martínez, R. Andrade, E. G. Birgin and J. M. Martínez, *J. Comput. Chem.*, 2009, **30**, 2157–2164.
42 S. Nosé, *J. Chem. Phys.*, 1984, **81**, 511–519.
43 W. G. Hoover, *Phys. Rev. A: At., Mol., Opt. Phys.*, 1985, **31**, 1695–1697.
44 M. Krishnan and S. Balasubramanian, *Phys. Rev. B: Condens. Matter Mater. Phys.*, 2003, **68**, 064304.
45 W. Humphrey, A. Dalke and K. Schulten, *J. Mol. Graphics*, 1996, **14**, 33–38.
46 Jmol: an open-source Java viewer for chemical structures in 3D. http://www.jmol.org/.
47 M. Harada, A. Yamanaka, M. Tanigaki and Y. Tada, *J. Chem. Phys.*, 1982, **76**, 1550–1556.
48 J.-P. Hansen and I. R. McDonald, *Theory of Simple Liquids*, Academic Press, 3rd edn, 2006.
49 M. G. Del Pópolo and G. A. Voth, *J. Phys. Chem. B*, 2004, **108**, 1744–1752.